iScience

CellPress
OPEN ACCESS

Article

Multiphase micro-computed tomography reconstructions provide dynamic respiratory function in a mouse lung fibrosis model

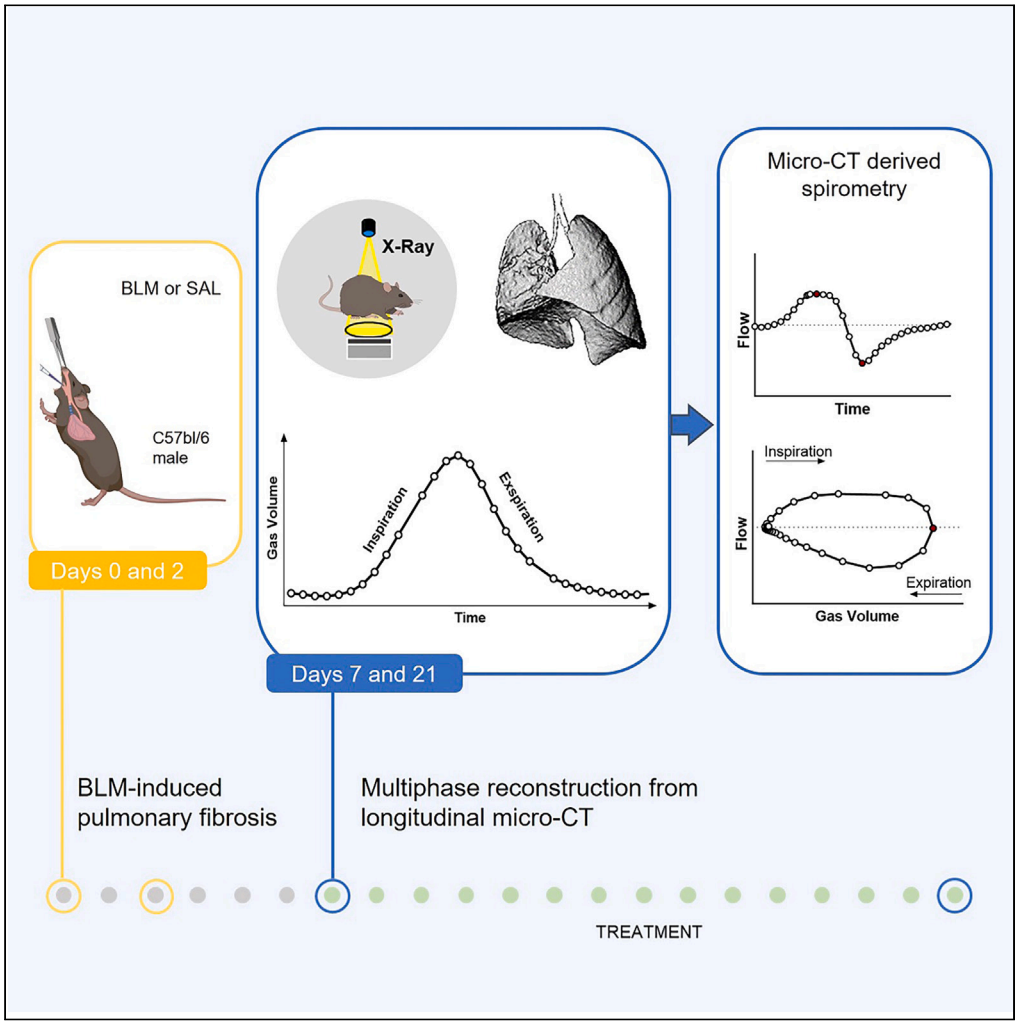

Francesca Pennati, Sasha Belenkov, Martina Buccardi, ..., Gino Villetti, Andrea Aliverti, Franco Fabio Stellari

fb.stellari@chiesi.com

Highlights

Multiphase reconstruction from micro-CT derives lung dynamics *in vivo*

4D micro-CT highlights obstructive and restrictive patterns of lung disease

4D micro-CT, as an alternative to spirometry, has strong clinical translation

Pennati et al., iScience *27*, 109262
March 15, 2024
https://doi.org/10.1016/j.isci.2024.109262

iScience

CellPress
OPEN ACCESS

Article

Multiphase micro-computed tomography reconstructions provide dynamic respiratory function in a mouse lung fibrosis model

Francesca Pennati,[1] Sasha Belenkov,[2] Martina Buccardi,[3] Erica Ferrini,[4] Nicola Sverzellati,[5] Gino Villetti,[6] Andrea Aliverti,[1] and Franco Fabio Stellari[6,7,*]

SUMMARY

Micro-computed tomography derived functional biomarkers used in lung disease research can significantly complement end-stage histomorphometric measures while also allowing for longitudinal studies. However, no approach for visualizing lung dynamics across a full respiratory cycle has yet been described. Using bleomycin-induced lung fibrosis and the antifibrotic drug nintedanib as a test model, we implemented a four-dimensional (4D) micro-CT imaging approach consisting of 30 reconstructed volumes per respiratory cycle, coupled with deep-learning-assisted segmentation of lung volumes. 4D micro-CT provided an accurate description of inhalatory and exhalatory lung dynamics under resting conditions and revealed an inflammation-related obstructive pattern at day 7, followed by a restrictive pattern associated with fibrosis development at day 21. A milder restriction and fibrotic pathology resulted from nintedanib treatment. The similarity of 4D micro-CT data with those produced by diagnostic measurements, also points to its great potential as an exploratory tool for the discovery of clinically relevant therapeutic compounds.

INTRODUCTION

Idiopathic pulmonary fibrosis (IPF) is a progressive fibrotic lung disease that ultimately leads to respiratory failure. To date, only two pharmacologic treatments are available, with limited efficacy on patients.[1] Although the number of preclinical studies to identify new antifibrotic drugs is increasing, the accurate measurement of lung function to assess drug efficacy in preclinical trials remains a critical issue.[2]

In humans, changes in lung function are usually based on spirometric measurements,[3–5] whereas in animal models, commercially available devices for measuring lung function are invasive and not suitable for reproducible repeated measurements, which limits their use for endpoint measurements.[2] As the longitudinal evaluation of disease progression in individual animals is a key requirement for functionally relevant studies of lung pathophysiology and response to therapy, lung imaging by micro-computed tomography (micro-CT) is establishing itself as the gold standard for the noninvasive assessment of changes in lung function.[6,7] The longitudinal evaluation capabilities of micro-CT (i.e., the possibility to perform the same measurements at multiple time-points in the same animal) also allow a considerable animal sparing, in compliance with the 3Rs (refinement, replacement, and reduction) goals for animal protection.[8]

Although the actual trade-off between experimental control, measurement sensitivity and invasiveness are still debated,[7,9] the usage and range of applications of micro-CT for noninvasive lung imaging has steadily increased over the last decade. Synchronized micro-CT imaging of free-breathing mice has been successfully employed to obtain three-dimensional tomographic data of the lungs at specific respiratory phases. Synchronization can be performed prospectively (i.e., with image acquisition triggered at specific respiratory phases during scanning), or retrospectively (i.e., with post-acquisition sorting of micro-CT images according to their respiratory phases). Several functional biomarkers derived from micro-CT density measurements performed at one respiratory volume have been introduced in recent years. These include, for example, the lung volume of trapped air,[10] hyperdense tissue[11] and mean lung density.[12,13] More accurate approaches based on the analysis of tissue density distribution have also been proposed to quantify the regional distribution of aeration compartments.[14,15] Despite an undeniable advance in the acquisition of functional and regional ventilation data from micro-CT images recorded at both end-expiratory and end-inspiratory phases,[16–19] a full representation of lung dynamics during an entire breath cycle has yet not been achieved.

[1]Dipartimento di Elettronica, Informazione e Bioingegneria, Politecnico di Milano, Milano, Italy
[2]PerkinElmer, Inc, Waltham, MA, USA
[3]Department of Mathematical, Physical and Computer Sciences, University of Parma, Parma, Italy
[4]Department of Veterinary Science, University of Parma, Parma, Italy
[5]Department of Medicine and Surgery, University of Parma, Parma, Italy
[6]Pharmacology and Toxicology Department Corporate Pre-Clinical R&D, Chiesi Farmaceutici S.p.A., Parma, Italy
[7]Lead contact
*Correspondence: fb.stellari@chiesi.com
https://doi.org/10.1016/j.isci.2024.109262

The aim of the present work was thus to find out whether multiphase reconstruction of four-dimensional (4D) micro-CT images (the fourth dimension being multiple observation times) can allow to fill this gap by introducing a post-processing method for full respiratory cycle reconstruction and dynamic functional analysis, with the derivation of micro-CT-based flow-volume loops, as those derived in clinical pulmonary function tests. The driving motivation for our study is to use *in vivo* micro-CT to develop functional assessment metrics during free tidal breathing, that can potentially lead to a better match between experimental methods in the preclinical and clinical setting. As a proof-of-concept testing, we longitudinally measured air volumes and flows from 4D micro-CT imaging in healthy and BLM-treated fibrotic mice as well as response to treatment with the human use-approved antifibrotic drug nintedanib (NINT). Our data indicate that 4D micro-CT imaging, which consists of approximately 30 reconstructed volumes per respiratory cycle, can indeed provide more comprehensive physiopathological information on lung motion during tidal breathing. In addition, the parameters derived from the multiphase reconstruction of micro-CT images, because of the fairly close resemblance of its output data with those typically produced by clinical pulmonary function tests, can represent an invaluable tool for the preclinical discovery of novel clinically relevant therapeutic compounds.

RESULTS

4D micro-CT images

Multiphase reconstructions closely representing the respiratory phases associated to an entire breathing cycle were successfully obtained at 16-millisecond time intervals in all tested mice (see Figure 1 for technical details on the reconstruction procedure). Representative mid-thorax coronal slices acquired at end-expiration/end-inspiration in saline controls (SAL), BLM- and BLM+nintedanib (NINT)-treated mice at day 7 and day 21 are shown in Figure 2. Both at day 7 and day 21, the SAL control displayed a uniform reduction in parenchymal density from end-expiratory to end-inspiratory phases, which reflects the increase in the gas fraction at end-inspiration compared to end-expiration. Under identical imaging conditions, a patchy reduction in parenchymal density with the appearance of ground glass opacities were observed in BLM and NINT mice at day 7, with the appearance of consolidations at day 21, both characterized by a diffuse and heterogeneous distribution.

Micro-CT-derived breathing pattern

Ventilatory pattern parameters measured during tidal breathing significantly differed between the three groups, with significant differences in breathing frequency, timing and duty cycle on day 7, and differences in tidal volume and mean inspiratory flow on day 21 (Table 1). On day 7, the BLM mice displayed a lowered breathing frequency compared to the SAL controls ($p = 0.038$) and a lower minute ventilation (median values 22.7 vs. 30.6; $p = 0.005$). The decreased inspiratory and increased expiratory times compared to the SAL controls also resulted in a lower duty cycle (median values 0.28 vs. 0.42; $p = 0.003$). On day 21, BLM and NINT mice had lower tidal volumes and mean inspiratory flows compared to controls, but with a normal breathing frequency and total respiratory cycle time.

Figure 3A shows the relationship between tidal volume and respiratory rate in the different groups. On day 7, BLM mice displayed a reduced minute ventilation, which remained essentially unchanged till day 21. A similarly reduced respiratory rate was observed in the NINT group at day 21. This behavior likely results from two opposite effects: a marked decrease of the breathing rate at day 7, and a similar decrease of tidal volume at day 21. Considering minute ventilation as the product of mean inspiratory flow (V_T/t_I) and duty cycle (t_I/T_{TOT}) (Figure 3B), it appears that the reduced minute ventilation in the BLM group is the result of the significantly lower duty cycle observed at day 7. On day 21, the duty cycle returned to normal values, with the lowered minute ventilation now resulting from a reduced mean inspiratory flow in both the BLM and NINT groups compared to SAL control mice, which displayed very similar values at both time-points.

Micro-CT-derived flow-volume loops

Flow-volume loops at day 7 and 21 are reported in Figure 4 as median curves for each group (*black curves*) both individually for each mouse (*gray curves*). At day 7, the BLM group featured an appreciable variation of the spontaneous expiratory flow-volume curve compared to the SAL controls, with a more concave shape resulting from an earlier peak of expiratory flow (at approximately 33 msec and 41 msec, respectively; $p = 0.02$), that was followed by a rapid flow decline. Altogether, a reduction of both the peak expiratory flow and of the flow values measured at the different volumes was apparent in the expiratory flow-volume curve of the BLM mice. On day 21, the expiratory loop concavity was no longer visible in the BLM and the NINT groups, but the loops remained reduced compared to those of the SAL controls, mainly due to reduced volumes.

All volume and flow variables for the three groups are reported in Table 2. On day 7, the BLM group displayed significantly lowered peak tidal expiratory ($p < 0.001$) and mean expiratory ($p < 0.001$) flows compared to the SAL controls. A significantly lower ($p = 0.033$) loop area, caused by a decrease in the expiratory loop area ($p < 0.001$), was also apparent at this time. On day 21, both the BLM and the NINT groups displayed significantly reduced peak tidal expiratory ($p = 0.002$ and $p = 0.004$, respectively), mean inspiratory ($p = 0.007$ and $p = 0.011$, respectively) and mean expiratory ($p = 0.002$ for both groups) flows compared to SAL control mice. In the BLM and NINT groups, loop areas were also significantly shrunk ($p < 0.001$ and $p = 0.004$, respectively) as a consequence of reduced inspiratory ($p = 0.002$ and $p = 0.017$, respectively) and reduced expiratory ($p < 0.001$ and $p = 0.002$, respectively) loops. Interestingly, separate analysis of the two lung lobes revealed a significant tidal volume difference between the BLM and the NINT groups ($p = 0.01$) at the level of the right lung (Tables S1 and S2).

Lung function measurements

BLM mice showed a significant decrease in IC ($p = 0.02$) and Cst ($p = 0.008$) compared to saline controls (Figures 5A and 5B). The trend toward a restrictive physiology of the BLM group, is also associated with a tendency toward higher tissue elastance and lower shape constant

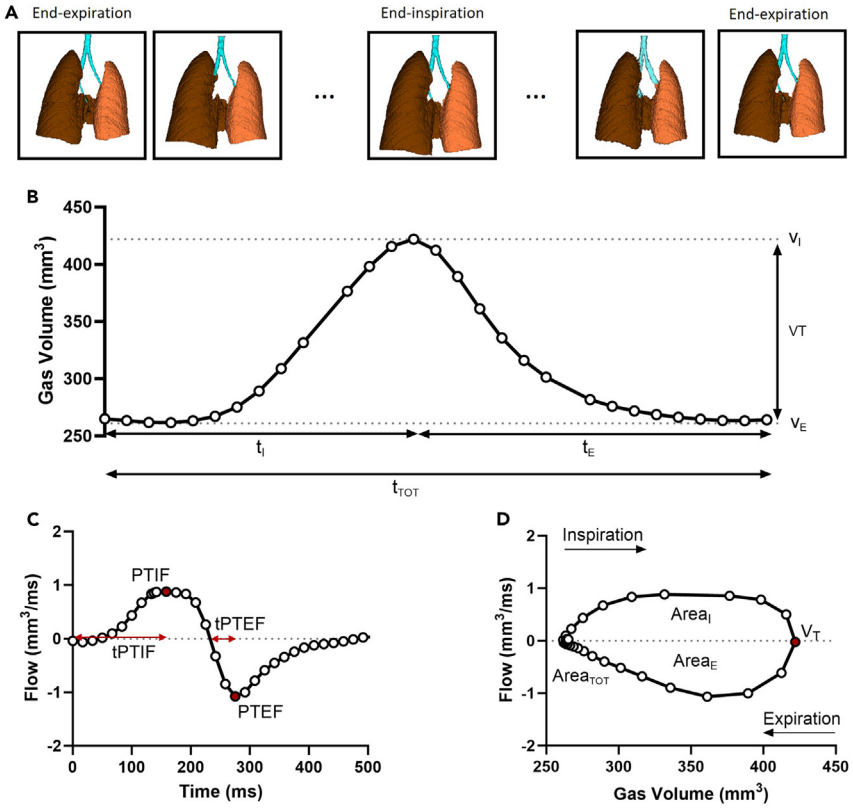

Figure 1. Multiphase reconstruction and extraction of dynamic respiratory function parameters

(A) Reconstructed respiratory phases in a representative mouse, with superimposed binary masks of the left and the right lung.

(B) The gas volume is calculated from each respiratory phase along the whole breathing cycle. The resulting time-varying scattered points are fitted into a continuous curve, reflecting the dynamic change of the amount of air that was breathed during the respiratory cycle.

(C) The gas flow calculated as the 1st derivative of the gas volume curve.

(D) Tidal breath flow-volume loop obtained by plotting the flow curve versus the gas volume. V_I, tidal volume; V_E, end-expiratory tidal volume; V_T, tidal volume; t_{TOT}, respiratory cycle length; t_I, inspiratory time; t_E, expiratory time; PTIF, peak tidal inspiratory flow; tPTIF, time to peak tidal inspiratory flow; PTEF, peak tidal expiratory flow; tPTEF, time to peak tidal expiratory flow; $Area_I$, inspiratory loop area; $Area_E$, expiratory loop area; $Area_{TOT}$, total loop area.

(Figure S2). Spearman correlation analyses between μCT-derived functional measurements and PFT outcomes showed significant correlations across multiple comparisons (Figure 5C), particularly between μCT-derived volume and flow parameters, and measures of IC and tissue distensibility.

Histological assessment of lung fibrosis

A subset of mice, both treated and controls, was sacrificed at days 7 and 21. For each group, representative fields stained with H&E and TM are shown in Figure 6. At day 7, BLM mice lungs were found to be swollen compared to the SAL controls (Figure S3) with a significant increase of both the BALF inflammatory infiltrate ($p = 0.012$) and the Ashcroft score ($p < 0.0001$). Inflammation decreased in the BLM group at day 21, but the Ashcroft score remained significantly higher than that of the SAL controls ($p < 0.0001$) due to the intense collagen deposition in the extracellular matrix that accompanied fibrosis development. NINT treatment reduced the severity of fibrotic lesions at day 21 ($p = 0.018$) and lowered the pulmonary WBC infiltrate, albeit not significantly compared to the BLM-only group.

As revealed by correlation analysis of respiratory dynamics and histomorphometric parameters, the Ashcroft score negatively correlated with end-inspiratory gas ($r = -0.60$, $p = 0.006$) and tidal ($r = -0.64$, $p = 0.002$) volumes. Notably, we also found a moderate negative correlation between the Ashcroft score and the total area ($r = -0.51$, $p = 0.02$), the inspiratory area ($r = -0.52$, $p = 0.02$) and the expiratory area ($r = -0.54$, $p = 0.01$) loops (Figure S4).

DISCUSSION

Micro-CT is a valuable tool for the noninvasive, longitudinal investigation of pulmonary disease progression and response to therapy. In the present study, we evaluated the spatial resolution and diagnostic potential of multiphase micro-CT applied to free-breathing mice to assess the dynamic respiratory function in a murine model of BLM-induced lung fibrosis. The novelty of this study is 2-fold. First, using a 4-min

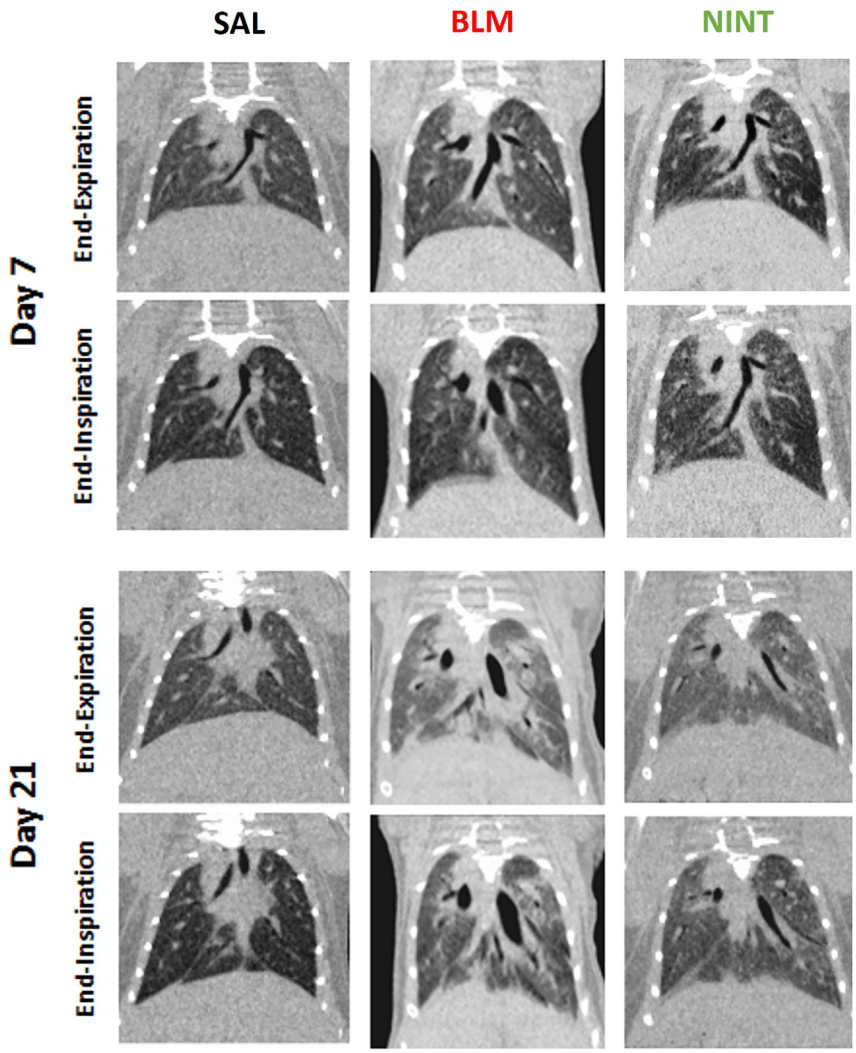

Figure 2. Representative multiphase images reconstructed at end inspiration and end expiration

Representative mid-thorax coronal slices at end-expiration and end-inspiration in a representative saline (SAL, first column), bleomycin (BLM, second column) and nintedanib-treated mouse (NINT, third column), acquired on day 7 and 21. From end-expiration to end-inspiration, images show reduced parenchymal density, due to increased gas fraction. The bleomycin and the nintedanib-treated mice display heterogeneously distributed ground glass opacities on day 7, and consolidations on day 21.

scanning protocol coupled with a deep learning system to automatically segment lung volumes, images from the entire respiratory cycle are reconstructed and analyzed, whereas current micro-CT imaging approaches are limited to the reconstruction and the analysis of a few respiratory phases. Second, the time-varying change in micro-CT-gas volume over the entire respiratory cycle is used to calculate the slope of gas volume (i.e., flow) during inspiration and expiration. Plotting flow as a function of gas volume allows the derivation of flow volume loops, similar to those obtained in clinical pulmonary function tests. These parameters describing respiration dynamics allowed a detailed longitudinal characterization of lung dysfunction, which highlighted an obstructive pattern causally related to the acute inflammatory response to BLM-instillation at day 7 and a restrictive pattern associated with fibrosis development at day 21.[20,21] Multiphase micro-CT also allowed to monitor the effect of treatment with the human use–approved drug nintedanib, which resulted in a milder restriction and a reduced fibrotic tissue formation. Comparison of micro-CT functional outcomes with postmortem histomorphometric endpoints revealed an overall good correlation between collagen deposition and functional impairment. Multiphase micro-CT, which is amenable to translation to other animal models and much closer to clinical diagnostic procedures than histomorphometric measurements, thus lends itself as an effective tool for a deeper understanding of the pathophysiology underlying different models of lung disease and the mode of action of new candidate drugs.

In the BLM group, reduced minute ventilation is appreciable both at day 7 and day 21, but likely results from different pathological responses. The reduced inspiratory duty cycle and longer expiratory times accompanied by reduced expiratory flows observed at day 7 strongly suggest an obstructive event, likely associated to the acute inflammatory reaction caused by BLM.[20,21] This interpretation is consistent with

Table 1. Ventilatory pattern parameters from multiphase micro-CT

	7 days		21 days		
	SAL (n = 6)	BLM (n = 16)	SAL (n = −10)	BLM (n = 16)	NINT (n = 10)
V_T (mm^3)	193.8 (189.6-198-6)	158.3 (147.8–197.3)	198.2 (172.0–203.5)	149.2 (124.0–154.7)***	156.1 (137.5–182.3)*
t_{TOT} (ms)	377.2 (368.8–392.8)	445.9 (399.0–511.6)*	375.1 (363.6–390.7)	383.4 (321.9–455.3)	406.3 (385.5–520.9)
t_I(ms)	158.4 (152.1–163.6)	133.4 (122.0–144.8)***	156.3 (149.0–168.8)	152.1 (130.2–181.3)	158.4 (144.8–212.5)
t_E(ms)	225.0 (208.4–230.3)	318.8 (261.5–383.4)**	210.5 (203.2–228.2)	223.0 (185.5–233.4)	241.7 (214.6–292.8)
Duty Cycle, t_I/t_{TOT} (%)	0.42 (0.40–0.43)	0.28 (0.25–0.32)**	0.43 (0.40–0.45)	0.41 (0.38–0.45)	0.41 (0.38–0.43)
RR (br/min)	159.1 (152.8–162.7)	134.6 (117.3–150.5)*	160.0 (153.6–165.0)	156.5 (131.8–186.5)	147.7 (115.2–155.7)
Min. Ventilation (cm^3/min)	30.6 (30.0–31.3)	22.7 (19.8–25.5)**	31.8 (27.1–33.5)	23.0 (18.2–26.7)**	21.4 (19.5–23.4)**
V_T/t_I(mm^3/ms)	1.24 (1.19–1.28)	1.29 (1.01–1.51)	1.23 (1.16–1.30)	0.97 (0.79–1.10)**	0.88 (0.82–1.07)*

Ventilatory pattern during tidal breathing in saline (SAL), bleomycin (BLM) and nintedanib-treated (NINT) mice, on day 7 and day 21. VT, tidal volume; tTOT, total respiratory cycle time; tI, inspiratory time; tE, expiratory time; RR, Respiratory rate. *: $p < 0.05$, **: $p < 0.01$, ***: $p < 0.001$, compared to SAL.

the results of a previous functional micro-CT study, which highlighted a decreased ventilation at day 7, in the presence of a relatively small percentage of fibrosis.[16] On day 21, instead, multiple time variable values were recovered in the BLM group, which, however, displayed reduced volumes and flows, both in inspiration and expiration, reflecting the restrictive pattern associated with the development of fibrosis. In keeping with the multiphase micro-CT results, histological *ex vivo* quantification of the Ashcroft score revealed a worsening of fibrosis from day 7 to day 21. The Ashcroft score increased significantly already at day 7 due to an increase in the inflammatory infiltrate as evidenced by BAL fluid cell counts and H&E staining. Also, at day 7, TM staining only evidenced newly formed collagen deposits in the lungs of BLM mice, which represent a typical feature of early fibrosis. At day 21, instead, the appearance of single fibrotic masses observed at day 7 evolved into confluent conglomerates of substitutive collagen with alveolar space alterations due to fibrotic proliferation and marked the transition to established fibrosis, concomitantly with inflammation decline.[22] In nintedanib-treated animals, a restrictive pattern was also detected by multiphase micro-CT at day 21, but of lower severity compared to that of BLM-only mice, as confirmed by histological data. This NINT alleviated phenotype became more evident when the lung lobes were separately investigated. Specifically, and in accordance with previous data, the difference in tidal volume between BLM-only and NINT animals was maximal, and with a stronger drug-modified phenotype in the more severe lung fibrosis, suggesting that harsher lesions might be more responsive to the pharmacological treatment.[18] Nintedanib has been shown in clinical studies to mitigate disease progression by lowering the annual FVC decrease and reducing the incidence of acute exacerbations,[5,23] while serious adverse effects have been reported.[24] In the current investigation, respiratory dynamic measures in NINT treated mice were milder but not-significantly different compared to BLM group. Although we acknowledge the current animal model's limitations to properly modeling the heterogeneous process of fibrosis,[25,26] we note that our parameters originated under tidal free breathing conditions, which may slightly underestimate the full dynamic of the lung, when compared to a maximal inspiratory maneuver, but may also better represent the physiological breathing conditions.

It is also important to note that the free-breathing scanning protocol, which does not require animal intubation and forced ventilation, allows to study breathing dynamics longitudinally under unperturbed physiological conditions, as opposed to the pre-set respiratory conditions imposed by mechanical ventilation. Similar limitations apply to other techniques employed to infer respiratory parameters in the preclinical setting, such as forced vital capacity (FVC) and forced expiratory volume in the first 0.1 s ($FEV_{0.1}$), which also require mice intubation with the inherent risk of potentially confusing experimental artifacts.[27]

A fairly robust structure-function relationship was highlighted by the correlation observed between histological and functional parameters, with lungs characterized by a high collagen content displaying lower gas content and volume-flow loops on micro-CT. Following bleomycin administration, the histological evidence of acute inflammation in the early stages was associated with expiratory flow limitation. At later time-points, inflammation is succeeded by fibrosis, with increased collagen deposition associated with lung volume reduction. Compared to histomorphometric measurements, micro-CT allows the spatial 3D assessment of the entire lung, enabling longitudinal monitoring of disease progression upon incorporation of observation time as a fourth dimension. Thus, at least in early stage investigations or high/mid throughput compound screenings, this may offset the lack of detailed cellular and molecular information, which can be provided on-demand (i.e., at specific predefined time-points) by complementary and more focused histological analyses.

In preclinical models, the differentiation between obstructive and restrictive lung disease is usually performed in anesthetized and tracheotomized animals at endpoint, with the use of flexiVent systems, which provide the most detailed set of lung functional parameters.[2] As expected, the BLM-induced tissue remodeling, with increased collagen deposition, resulted in decreased inspiratory capacity and lung compliance. The reduced ability of the lungs to expand and the increased tissue stiffness were correlated with the reduced volumes and flows assessed by micro-CT, suggesting that the differentiation between obstructive and restrictive physiological patterns can be achieved *in vivo* and in free-breathing mice by 4D micro-CT imaging performed in the same animal at multiple time-points. Moreover, cumulative readouts such as those produced by the above-mentioned invasive systems may underestimate the actual extent of lung disease in the case of a localized pathology with compensatory effects by unaffected nearby regions aimed at maintaining an adequate level of overall ventilation.[16]

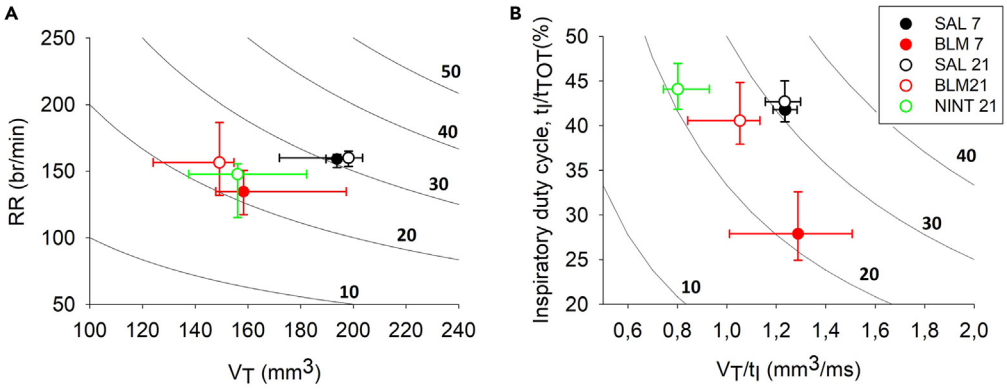

Figure 3. Breathing pattern derived from multiphase micro-CT

(A) Relationship between the median values (25th-75th percentile) of tidal volume (V_T, x axis) and respiratory rate (RR, y axis) in saline (SAL, black), bleomycin (BLM, red) and nintedanib-treated (NINT, green) groups on day 7 (filled circles) and day 21 (open circles). Lines represent the isopleths of different levels of minute ventilation ($\dot{V}$) from 10 to 50 mm^3/min, according to the relation $\dot{V} = V_T * RR$.

(B) Relationship between the median values (25th-75th percentile) of inspiratory flow (V_T/t_I, x axis) and duty cycle (t_I/T_{TOT}, y axis) in saline (SAL, black), bleomycin (BLM, red) and nintedanib-treated (NINT, green) groups on day 7 (filled circles) and day 21 (open circles).). Lines represent the isopleths of different levels of minute ventilation ($\dot{V}$) from 10 to 50 cm^3/min, according to the relation $\dot{V} = \frac{V_T}{t_I} * \frac{t_I}{t_{TOT}}$.

In contrast to the numerous techniques available to assess either lung structure or lung function, as histomorphometry analysis or pulmonary function tests, the combination of structural and functional imaging offers the unique ability to assess structural and functional changes simultaneously, allowing identification of the origin of the functional changes, which may improve our understanding of structure–function relationships in the earliest stages of disease.

Functional lung imaging enables regional quantification of lung function and provides more sensitive spatial information compared to global measurements at the openings of the large airways. Registration-based algorithms to assess regional ventilation have been proposed based on respiratory-gated micro-CT.[28] More sophisticated methods have been introduced that infer local airflow at each branch in the segmented airway tree by measuring lung motion in conjunction with airway structure.[29] In the present study, we proposed a simpler approach to derive functional metrics that can separate the left and right contributions to whole lung function. Further development of our deep learning segmentation pipeline with lung lobar delineation could enable the assessment of lobar ventilation. Although higher resolution images would provide more structural detail,[30] this would require prolonged acquisition and anesthesia, which may result in respiratory rate depression, which could affect our estimates.

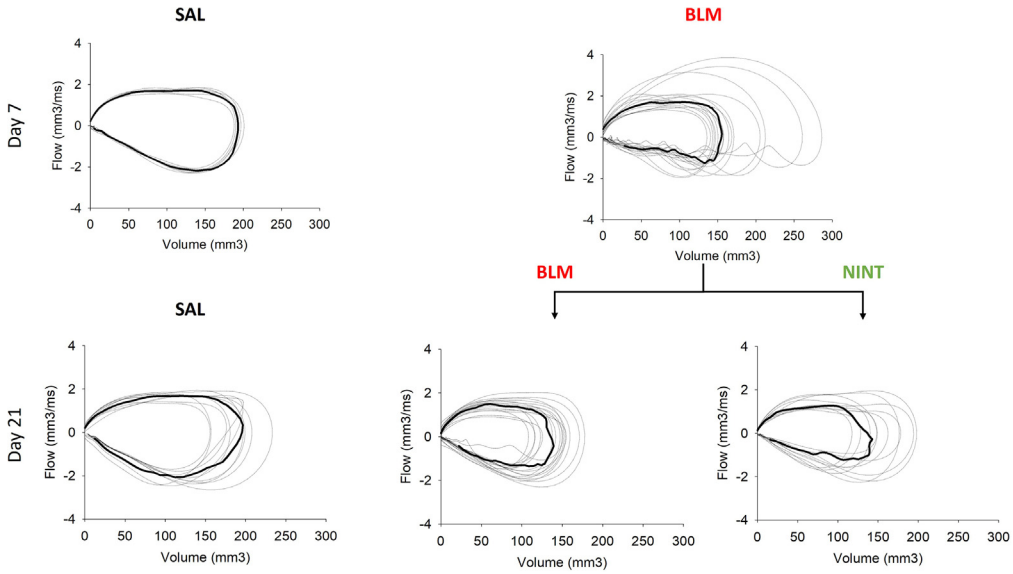

Figure 4. Flow-volume loops derived from multiphase micro-CT

Individual (thin line) and overall group (solid line) flow-volume loops in saline (SAL, left), bleomycin (BLM, middle) and nintedanib-treated (NINT, right) groups, on day 7 (top row) and 21 (bottom row).

Table 2. Volume-flow parameters from multiphase micro-CT

	7 days		21 days		
	Saline (n = 6)	BLM (n = 16)	Saline (n = 10)	BLM (n = 16)	NTD (n = 10)
V_I (mm^3)	477.5 (449.0–505.7)	472.6 (434.5–538.1)	475.5 (439.1–529.5)	405.5 (350.7–440.1)*	464.0 (386.7–492.6)
V_E (mm^3)	283.9 (255.5–306.1)	297.2 (274.0–334.9)	268.6 (263.6–323.6)	250.7 (218.8–295.4)	288.6 (256.9–321.7)
PTIF (mm^3/ms)	1.8 (1.7–1.8)	1.9 (1.5–2.1)	1.7 (1.6–1.8)	1.5 (1.2–1.7)	1.3 (1.2–1.8)
MTIF (mm^3/ms)	1.2 (1.2–1.3)	1.2 (1.0–1.5)	1.2 (1.1–1.3)	0.9 (0.8–1.1)**	0.9 (0.8–1.0)*
Time to PTIF (ms)	91.7 (79.2–113.6)	83.4 (59.4–91.7)	93.8 (77.1–110.4)	83.4 (66.7–106.3)	97.9 (85.4–107.3)
PTEF(mm^3/ms)	2.2 (2.1–2.3)	1.5 (1.3–1.9)***	2.3 (1.9–2.4)	1.7 (1.4–1.9)**	1.6 (1.5–2.0)**
MTEF (mm^3/ms)	0.9 (0.8–0.9)	0.5 (0.5–0.7)***	0.9 (0.7–1.0)	0.6 (0.5–0.7)**	0.6 (0.5–0.6)**
Time to PTEF(ms)	41.7 (37.5–41.7)	33.3 (30.2–39.6)*	41.7 (37.5–41.7)	37.5 (37.5–41.7)	41.7 (37.5–46.9)
$Area_{TOT}$ (mL^2/ms)	0.56 (0.54–0.58)	0.37 (0.29–0.52)*	0.59 (0.42–0.61)	0.33 (0.23–0.41)***	0.31 (0.28–0.47)**
$Area_I$ (mL^2/ms)	0.29 (0.26–0.30)	0.23 (0.19–0.33)	0.28 (0.22–0.31)	0.17 (0.13–0.21)***	0.17 (0.14–0.23)**
$Area_E$ (mL^2/ms)	0.28 (0.26–0.29)	0.13 (0.11–0.19)***	0.30 (0.20–0.32)	0.16 (0.11–0.20)***	0.16 (0.14–0.24)**

Volume-flow parameters during tidal breathing in saline (SAL), bleomycin (BLM) and the nintedanib-treated (NINT) mice on day 7 and day 21. VI, end-inspiratory volume, VE, end-expiratory volume, PTIF, peak tidal inspiratory flow; MTIF, mean tidal inspiratory flow; PTEF, peak tidal expiratory flow; MTEF, mean tidal expiratory flow; AreaTOT, total loop area; AreaI, inspiratory loop area; AreaE, expiratory loop area. *: $p < 0.05$, **: $p < 0.01$, ***: $p < 0.001$, compared to SAL.

The radiation dose delivered with a single respiratory-gated micro-CT acquisition is approximately 300 mGy,[31] which is about an order of magnitude below the doses for which adverse radiation effects have been reported in mouse lung.[32] Previous studies have shown that in healthy animals, repeated weekly or biweekly respiratory-gated μCT scans at about 800 mGy for 5 to 12 weeks have no radiotoxic effects on the lungs.[33] Accordingly, no regions of increased density on μCT scans were observed in the saline control group, nor were any cellular or architectural abnormalities attributable to irradiation detected by standard histologic analyses. In addition, none of the animals showed signs of systemic disturbance such as weight loss or behavioral changes during the study, indicating that the X-ray dose had no systemic side effects. Furthermore, we regularly performed experiments to support our R&D pipeline in which some saline and BLM animals were not CT-scanned, but at the end of the experiment all mice were euthanized, and the lungs were always excised for histological analysis. The pathologists never reported any unusual findings when comparing imaged and unimaged lungs.

The study provides a proof-of-concept documentation of the capabilities of 4D micro-CT as an *in vivo* diagnostic tool that can provide valuable functional parameters for preclinical pharmacological studies of lung disease. This approach represents a new and alternative way to spirometry, since similar parameters can be derived to explore the mechanical ventilation of the lung, however, corroborate by radiological features. The core micro-CT technology relies on standard imaging instrumentation and image processing procedures, which decrease the intra-extra experimental variability and make it easily transferrable, to other laboratories and to other lung disease-related

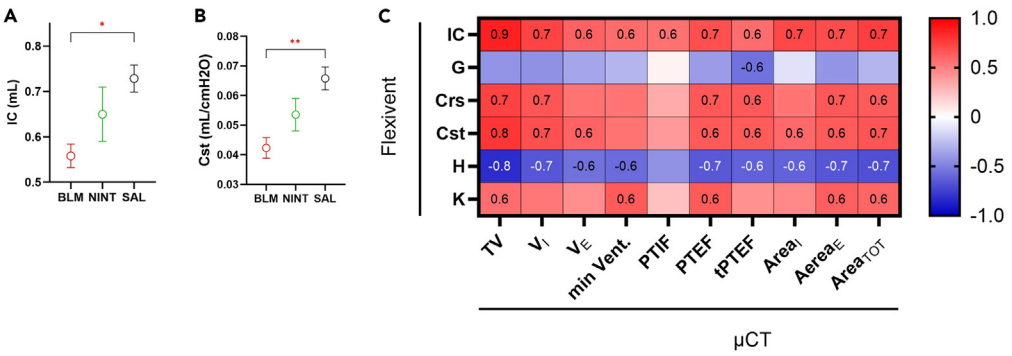

Figure 5. Lung function measurements by micro-CT imaging and by pulmonary function tests

Pulmonary function tests performed on day 21 in saline (SAL), bleomycin (BLM) and nintedanib-treated (NINT) animals. Inspiratory capacity (A) and static compliance (B) were significantly lower in BLM compared to SAL (respectively $p = 0.02$ and $p = 0.008$). Data are expressed as mean ± SD. One-way analysis of variance and Dunnett's multiple comparison post hoc test was applied to compare PFT outcome measures between groups.

(C) micro-CT and flexiVent data were correlated using a Spearman matrix. The color bar evidence high positive correlations in red, whereas negative trends are shown in blue. For each correlation the $R_{Spearman}$ has been reported in each box if significant. IC, inspiratory capacity; G, lung tissue damping; H, lung tissue elastance; Cst, static compliance; Crs, dynamic compliance.

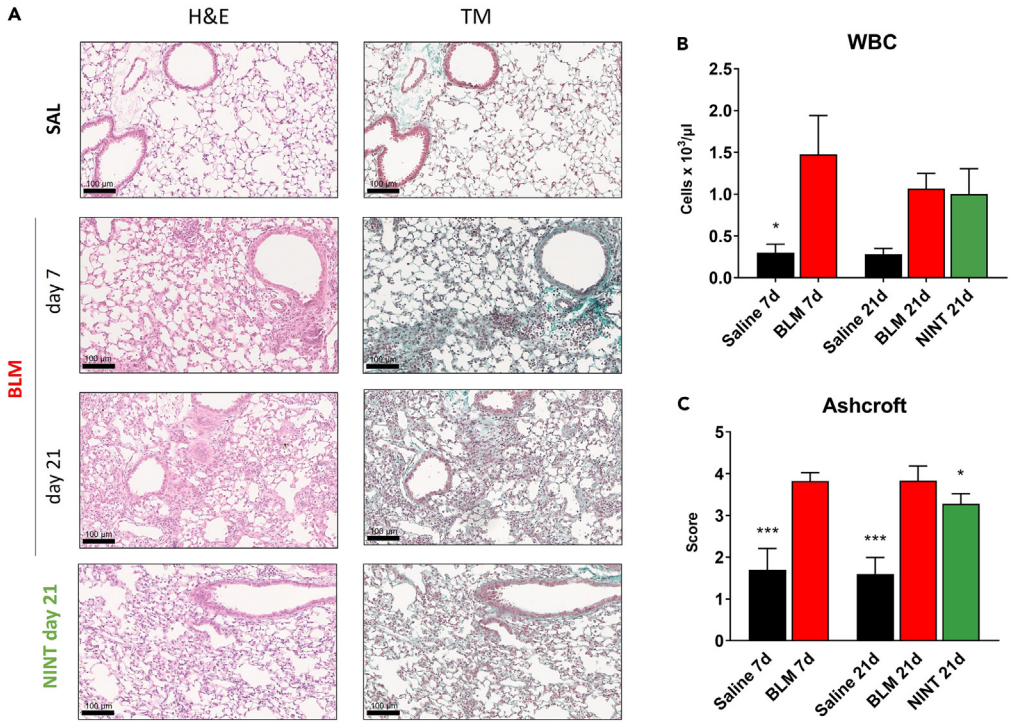

Figure 6. Histomorphometric analysis of lung fibrosis progression

(A) Histological assessment of fibrosis progression in the BLM model and nintedanib effect. a) Representative images (20X magnification, bar scale corresponds to 100µm) of Hematoxylin and eosin (H&E) and Masson's trichrome (TM) stained histological sections from representative saline control (SAL, black), bleomycin (BLM, red) and nintedanib-treated (NINT, green) mice.

(B) White blood cells (WBC) pulmonary infiltrate quantification for the three groups on the whole lungs, on day 7 and 21, with significantly lower values in the saline compared to the BLM group.

(C) Ashcroft score quantification for the three groups on the whole lungs, on day 7 and 21, with both saline and NINT groups showing lower values compared to BLM. Statistical significance of the differences between groups were calculated by One-way ANOVA followed by Tukey's test for multiple comparison (*$p < 0.05$; ***$p < 0.001$ vs. BLM group), separately at the two timepoints.

preclinical settings. We also believe that our approach has a high clinical translation potential, as it allows to investigate the therapeutic efficacy and mode of action of established or new candidate drugs on the basis of functional parameters that are very close to those utilized in clinical practice for the assessment of lung fibrosis.

Limitations of the study

Despite its promising results, the present study has some limitations. First, a relatively small number of animals was included in each group and not all of them were imaged at all time-points. Although each animal should be compared with its own baseline control to reduce intra-group variability, significant differences were also observed within individual groups, pointing to the high sensitivity of 4D micro-CT. We also note that the deep-learning algorithms utilized for segmentation of respiratory phases require access to cloud computing, which may not be easily accessible to all research groups. In addition, our study was conducted using the BLM-induced model of pulmonary fibrosis, whose clinical relevance is still controversial. Nevertheless, it is by far the most used preclinical model of human IPF, as it allows rapid, dose-dependent induction of a lung fibrosis phenotype with an acceptable level of reproducibility.[25,34] Interestingly, application of the proposed methodology to more advanced models of pulmonary fibrosis[35] may highlight the different dynamic response to fibrosis induction.

STAR★METHODS

Detailed methods are provided in the online version of this paper and include the following:

- KEY RESOURCES TABLE
- RESOURCE AVAILABILITY
  - Lead contact
  - Materials availability
  - Data and code availability

SUPPLEMENTAL INFORMATION

Supplemental information can be found online at https://doi.org/10.1016/j.isci.2024.109262.

ACKNOWLEDGMENTS

The authors thank Prof. Simone Ottonello (Department of Chemistry, Life Sciences and Environmental Sustainability, University of Parma, Italy) for the critical revision of the manuscript.

AUTHOR CONTRIBUTIONS

Conception and design of the study: F.P., S.B., A.A., and F.F.S.; acquisition, analysis, or interpretation of data: F.P., S.B., M.B., E.F., N.S., G.V., A.A., and F.F.S.; drafting the article: F.P., E.F., and F.F.S.; revising it critically for important intellectual content: F.P., S.B., M.B., E.F., N.S., G.V., A.A., and F.F.S. All authors read and approved the final manuscript.

DECLARATION OF INTERESTS

F.F.S. and G.V. are employees of Chiesi Farmaceutici S.p.A., that supported the research work. The remaining authors declare that the research was conducted in the absence of any commercial or financial relationships that could be perceived as a potential conflict of interest.

Received: August 29, 2023
Revised: December 13, 2023
Accepted: February 14, 2024
Published: February 16, 2024

REFERENCES

1. Richeldi, L., Collard, H.R., and Jones, M.G. (2017). Idiopathic pulmonary fibrosis. Lancet *389*, 1941–1952. https://doi.org/10.1016/S0140-6736(17)30866-8.
2. Jenkins, R.G., Moore, B.B., Chambers, R.C., Eickelberg, O., Königshoff, M., Kolb, M., Laurent, G.J., Nanthakumar, C.B., Olman, M.A., Pardo, A., et al. (2017). An official American thoracic society workshop report: Use of animal models for the preclinical assessment of potential therapies for pulmonary fibrosis. Am. J. Respir. Cell Mol. Biol. *56*, 667–679. https://doi.org/10.1165/rcmb.2017-0096ST.
3. Noble, P.W., Albera, C., Bradford, W.Z., Costabel, U., Glassberg, M.K., Kardatzke, D., King, T.E., Lancaster, L., Sahn, S.A., Szwarcberg, J., et al. (2011). Pirfenidone in patients with idiopathic pulmonary fibrosis (CAPACITY): two randomised trials. Lancet *377*, 1760–1769. https://doi.org/10.1016/S0140-6736(11)60405-4.
4. Lederer, D.J., Bradford, W.Z., Fagan, E.A., Glaspole, I., Glassberg, M.K., Glasscock, K.F., Kardatzke, D., King, T.E., Lancaster, L.H., Nathan, S.D., et al. (2015). Sensitivity Analyses of the Change in FVC in a Phase 3 Trial of Pirfenidone for Idiopathic Pulmonary Fibrosis. Chest *148*, 196–201. https://doi.org/10.1378/chest.14-2817.
5. Richeldi, L., du Bois, R.M., Raghu, G., Azuma, A., Brown, K.K., Costabel, U., Cottin, V., Flaherty, K.R., Hansell, D.M., Inoue, Y., et al. (2014). Efficacy and Safety of Nintedanib in Idiopathic Pulmonary Fibrosis. N. Engl. J. Med. *370*, 2071–2082. https://doi.org/10.1056/NEJMoa1402584.
6. Glaab, T., Taube, C., Braun, A., and Mitzner, W. (2007). Invasive and noninvasive methods for studying pulmonary function in mice. Respir. Res. *8*, 63. https://doi.org/10.1186/1465-9921-8-63.
7. Bates, J.H.T., and Irvin, C.G. (2003). Measuring lung function in mice: the phenotyping uncertainty principle. J. Appl. Physiol. *94*, 1297–1306. https://doi.org/10.1152/japplphysiol.00706.2002.
8. Wadman, M. (2023). FDA no longer has to require animal testing for new drugs. Science *379*, 127–128. https://doi.org/10.1126/science.adg6276.
9. Hoymann, H.G. (2012). Lung Function Measurements in Rodents in Safety Pharmacology Studies. Front. Pharmacol. *3*, 156. https://doi.org/10.3389/fphar.2012.00156.
10. de Langhe, E., Vande Velde, G., Hostens, J., Himmelreich, U., Nemery, B., Luyten, F.P., Vanoirbeek, J., and Lories, R.J. (2012). Quantification of lung fibrosis and emphysema in mice using automated micro-computed tomography. PLoS One *7*, e43123. https://doi.org/10.1371/journal.pone.0043123.
11. Namati, E., Thiesse, J., Sieren, J.C., Ross, A., Hoffman, E.A., and McLennan, G. (2010). Longitudinal assessment of lung cancer progression in the mouse using *in vivo* micro-CT imaging. Med. Phys. *37*, 4793–4805. https://doi.org/10.1118/1.3476454.
12. Vande Velde, G., Poelmans, J., De Langhe, E., Hillen, A., Vanoirbeek, J., Himmelreich, U., and Lories, R.J. (2016). Longitudinal micro-CT provides biomarkers of lung disease that can be used to assess the effect of therapy in preclinical mouse models, and reveal compensatory changes in lung volume. Dis. Model. Mech. *9*, 91–98. https://doi.org/10.1242/dmm.020321.
13. Shofer, S., Badea, C., Qi, Y., Potts, E., Foster, W.M., and Johnson, G.A. (2008). A micro-CT analysis of murine lung recruitment in bleomycin-induced lung injury. J. Appl. Physiol. *105*, 669–677. https://doi.org/10.1152/japplphysiol.00980.2007.
14. Mecozzi, L., Mambrini, M., Ruscitti, F., Ferrini, E., Ciccimarra, R., Ravanetti, F., Sverzellati, N., Silva, M., Ruffini, L., Belenkov, S., et al. (2020). In-vivo lung fibrosis staging in a bleomycin-mouse model: a new micro-CT guided densitometric approach. Sci. Rep. *10*, 118735. https://doi.org/10.1038/s41598-020-71293-3.
15. Vincenzi, E., Fantazzini, A., Basso, C., Barla, A., Odone, F., Leo, L., Mecozzi, L., Mambrini, M., Ferrini, E., Sverzellati, N., and Stellari, F.F. (2022). A fully automated deep learning

pipeline for micro-CT-imaging-based densitometry of lung fibrosis murine models. Respir. Res. *23*, 308. https://doi.org/10.1186/s12931-022-02236-x.

16. Pennati, F., Leo, L., Ferrini, E., Sverzellati, N., Bernardi, D., Stellari, F.F., and Aliverti, A. (2023). Micro-CT-derived ventilation biomarkers for the longitudinal assessment of pathology and response to therapy in a mouse model of lung fibrosis. Sci. Rep. *13*, 4462. https://doi.org/10.1038/s41598-023-30402-8.
17. Ford, N.L., Martin, E.L., Lewis, J.F., Veldhuizen, R.A.W., Drangova, M., and Holdsworth, D.W. (2007). In vivo characterization of lung morphology and function in anesthetized free-breathing mice using micro-computed tomography. J. Appl. Physiol. *102*, 2046–2055. https://doi.org/10.1152/japplphysiol.00629.2006.
18. Buccardi, M., Ferrini, E., Pennati, F., Vincenzi, E., Ledda, R.E., Grandi, A., Buseghin, D., Villetti, G., Sverzellati, N., Aliverti, A., and Stellari, F.F. (2023). A fully automated micro-CT deep learning approach for precision preclinical investigation of lung fibrosis progression and response to therapy. Respir. Res. *24*, 126. https://doi.org/10.1186/s12931-023-02432-3.
19. Ford, N.L., Nikolov, H.N., Norley, C.J.D., Thornton, M.M., Foster, P.J., Drangova, M., and Holdsworth, D.W. (2005). Prospective respiratory-gated micro-CT of free breathing rodents. Med. Phys. *32*, 2888–2898. https://doi.org/10.1118/1.2013007.
20. Ruscitti, F., Ravanetti, F., Essers, J., Ridwan, Y., Belenkov, S., Vos, W., Ferreira, F., KleinJan, A., Van Heijningen, P., Van Holsbeke, C., et al. (2017). Longitudinal assessment of bleomycin-induced lung fibrosis by Micro-CT correlates with histological evaluation in mice. Multidiscip. Respir. Med. *12*, 8–10. https://doi.org/10.1186/s40248-017-0089-0.
21. Stellari, F.F., Ruscitti, F., Pompilio, D., Ravanetti, F., Tebaldi, G., Macchi, F., Verna, A.E., Villetti, G., and Donofrio, G. (2017). Heterologous Matrix Metalloproteinase Gene Promoter Activity Allows In Vivo Real-time Imaging of Bleomycin-Induced Lung Fibrosis in Transiently Transgenized Mice. Front. Immunol. *8*, 199. https://doi.org/10.3389/fimmu.2017.00199.
22. Ruscitti, F., Ravanetti, F., Bertani, V., Ragionieri, L., Mecozzi, L., Sverzellati, N., Silva, M., Ruffini, L., Menozzi, V., Civelli, M., et al. (2020). Quantification of Lung Fibrosis in IPF-Like Mouse Model and Pharmacological Response to Treatment by Micro-Computed Tomography. Front. Pharmacol. *11*, 1117. https://doi.org/10.3389/fphar.2020.01117.
23. Richeldi, L., Costabel, U., Selman, M., Kim, D.S., Hansell, D.M., Nicholson, A.G., Brown, K.K., Flaherty, K.R., Noble, P.W., Raghu, G., et al. (2011). Efficacy of a Tyrosine Kinase Inhibitor in Idiopathic Pulmonary Fibrosis. N. Engl. J. Med. *365*, 1079–1087. https://doi.org/10.1056/NEJMoa1103690.
24. Podolanczuk, A.J., and Cottin, V. (2023). A Narrative Review of Real-World Data on the Safety of Nintedanib in Patients with Idiopathic Pulmonary Fibrosis. Adv. Ther. *40*, 2038–2050. https://doi.org/10.1007/s12325-023-02454-9.
25. Moeller, A., Ask, K., Warburton, D., Gauldie, J., and Kolb, M. (2008). The bleomycin animal model: A useful tool to investigate treatment options for idiopathic pulmonary fibrosis? Int. J. Biochem. Cell Biol. *40*, 362–382. https://doi.org/10.1016/J.BIOCEL.2007.08.011.
26. Scotton, C.J., and Chambers, R.C. (2010). Bleomycin revisited: towards a more representative model of IPF? Am. J. Physiol. Lung Cell Mol. Physiol. *299*, L439–L441. https://doi.org/10.1152/ajplung.00258.2010.
27. Bonnardel, E., Prevel, R., Campagnac, M., Dubreuil, M., Marthan, R., Berger, P., and Dupin, I. (2019). Determination of reliable lung function parameters in intubated mice. Respir. Res. *20*, 211. https://doi.org/10.1186/s12931-019-1177-9.
28. Pennati, F., Salito, C., and Aliverti, A. (2015). Registration of lung CT images acquired in different respiratory ranges with 4DCT and HRCT. In Proceedings of the Annual International Conference of the IEEE Engineering in Medicine and Biology Society (EMBS). https://doi.org/10.1109/EMBC.2015.7319007.
29. Stahr, C.S., Samarage, C.R., Donnelley, M., Farrow, N., Morgan, K.S., Zosky, G., Boucher, R.C., Siu, K.K.W., Mall, M.A., Parsons, D.W., et al. (2016). Quantification of heterogeneity in lung disease with image-based pulmonary function testing. Sci. Rep. *6*, 29438. https://doi.org/10.1038/srep29438.
30. Zhu, L., Duerr, J., Zhou-Suckow, Z., Wagner, W., Weinheimer, O., Salomon, J., Leitz, D., Konietzke, P., Yu, H., Ackermann, M., et al. (2022). μCT to quantify muco-obstructive lung disease and effects of neutrophil elastase knockout in mice. Am. J. Physiol. Lung Cell Mol. Physiol. *322*, L401–L411. https://doi.org/10.1152/ajplung.00341.2021.
31. Meganck, J.A., and Liu, B. (2017). Dosimetry in Micro-computed Tomography: a Review of the Measurement Methods, Impacts, and Characterization of the Quantum GX Imaging System. Mol. Imag. Biol. *19*, 499–511. https://doi.org/10.1007/s11307-016-1026-x.
32. Plathow, C., Li, M., Gong, P., Zieher, H., Kiessling, F., Peschke, P., Kauczor, H.-U., Abdollahi, A., and Huber, P.E. (2004). Computed Tomography Monitoring of Radiation-Induced Lung Fibrosis in Mice. Invest. Radiol. *39*, 600–609. https://doi.org/10.1097/01.rli.0000138134.89050.a5.
33. Vande Velde, G., De Langhe, E., Poelmans, J., Bruyndonckx, P., d'Agostino, E., Verbeken, E., Bogaerts, R., Lories, R., and Himmelreich, U. (2015). Longitudinal *in vivo* microcomputed tomography of mouse lungs: No evidence for radiotoxicity. Am. J. Physiol. Lung Cell Mol. Physiol. *309*, L271–L279. https://doi.org/10.1152/ajplung.00098.2015.
34. Liu, T., De Los Santos, F.G., and Phan, S.H. (2017). The bleomycin model of pulmonary fibrosis. Methods Mol. Biol. *1627*, 27–42. https://doi.org/10.1007/978-1-4939-7113-8_2/COVER.
35. Duerr, J., Leitz, D.H.W., Szczygiel, M., Dvornikov, D., Fraumann, S.G., Kreutz, C., Zadora, P.K., Seyhan Agircan, A., Konietzke, P., Engelmann, T.A., et al. (2020). Conditional deletion of Nedd4-2 in lung epithelial cells causes progressive pulmonary fibrosis in adult mice. Nat. Commun. *11*, 2012. https://doi.org/10.1038/s41467-020-15743-6.
36. Ferrini, E., Mecozzi, L., Corsi, L., Ragionieri, L., Donofrio, G., and Stellari, F.F. (2020). Alfaxalone and Dexmedetomidine as an Alternative to Gas Anesthesia for Micro-CT Lung Imaging in a Bleomycin-Induced Pulmonary Fibrosis Murine Model. Front. Vet. Sci. *7*, 588592. https://doi.org/10.3389/fvets.2020.588592.
37. Ferrini, E., Leo, L., Corsi, L., Catozzi, C., Salomone, F., Ragionieri, L., Pennati, F., and Stellari, F.F. (2021). A new anesthesia protocol enabling longitudinal lung function measurements in neonatal rabbits by micro-CT. Am. J. Physiol. Lung Cell Mol. Physiol. *321*, L1206–L1214. https://doi.org/10.1152/AJPLUNG.00328.2021.
38. van der Ent, C.K., Brackel, H.J., van der Laag, J., and Bogaard, J.M. (1996). Tidal breathing analysis as a measure of airway obstruction in children three years of age and older. Am. J. Respir. Crit. Care Med. *153*, 1253–1258. https://doi.org/10.1164/ajrccm.153.4.8616550.
39. Seddon, P.C., Davis, G.M., and Coates, A.L. (1996). Do tidal expiratory flow patterns reflect lung mechanics in infants? Am. J. Respir. Crit. Care Med. *153*, 1248–1252. https://doi.org/10.1164/ajrccm.153.4.8616549.
40. Stellari, F.F., Lavrentiadou, S., Ruscitti, F., Jacca, S., Franceschi, V., Civelli, M., Carnini, C., Villetti, G., and Donofrio, G. (2014). Enlightened Mannhemia haemolytica lung inflammation in bovinized mice. Vet. Res. *45*, 8. https://doi.org/10.1186/1297-9716-45-8.
41. Ashcroft, T., Simpson, J.M., and Timbrell, V. (1988). Simple method of estimating severity of pulmonary fibrosis on a numerical scale. J. Clin. Pathol. *41*, 467–470. https://doi.org/10.1136/jcp.41.4.467.
42. Hübner, R.H., Gitter, W., El Mokhtari, N.E., Mathiak, M., Both, M., Bolte, H., Freitag-Wolf, S., and Bewig, B. (2008). Standardized quantification of pulmonary fibrosis in histological samples. Biotechniques *44*, 507–517. https://doi.org/10.2144/000112729.
43. Grandi, A., Ferrini, E., Mecozzi, L., Ciccimarra, R., Zoboli, M., Leo, L., Khalajzeyqami, Z., Kleinjan, A., Löwik, C.W.G.M., Donofrio, G., et al. (2023). Indocyanine-enhanced mouse model of bleomycin-induced lung fibrosis with hallmarks of progressive emphysema. Am. J. Physiol. Lung Cell Mol. Physiol. *324*, L211–L227. https://doi.org/10.1152/ajplung.00180.2022.

STAR★METHODS

KEY RESOURCES TABLE

REAGENT or RESOURCE	SOURCE	IDENTIFIER
Chemicals, peptides, and recombinant proteins		
Bleomycin Baxter 15'000 I.U.	Baxter Oncology GmbH, Germany	N/A
Nintedanib Ethanesulfonate Salt	Carbosynth Limited, Compton, UK	FD71497
Tween 80	Sigma-Aldrich	P1754
Hank's balanced salt solution	Thermo Fisher Scientific	14175053
PBS pH 7.4 (1X)	Thermo Fisher Scientific	10010056
Ethylenediaminetetraacetic acid disodium salt solution (EDTA)	Sigma-Aldrich	E7889
HEPES (1M)	Sigma-Aldrich	83264
Formaldehyde solution 4% buffered, pH 6.	Sigma-Aldrich	100496
Critical commercial assays		
Masson's trichrome kit	Histo-Line Laboratories	N/A
Hematoxylin and Eosin kit	Histo-Line Laboratories	N/A
Experimental models: Organisms/strains		
C57Bl/6 mice, 7-8 weeks old, female adult	Envigo, San Pietro al Natisone, Udine, Italy	N/A
Software and algorithms		
GraphPad Prism 7	https://www.graphpad.com/scientificsoftware/prism/	GraphPad Prism
Matlab R2019a	https://se.mathworks.com/products/matlab.html	Matlab

RESOURCE AVAILABILITY

Lead contact

Further information and requests for resources should be directed to and will be fulfilled by the lead contact, Franco F. Stellari (fb.stellari@chiesi.com).

Materials availability

This study did not generate new unique reagents.

Data and code availability

- All data reported in this paper are available for non-commercial use from the authors upon reasonable request and with necessary data access agreements in place.
- Original code used in the analysis of micro-CT imaging data are available from the lead contact upon request.
- Any additional information required to reanalyze the data reported in this paper is available from the lead contact upon request.

EXPERIMENTAL MODEL AND STUDY PARTICIPANT DETAILS

All animal experiments described herein were approved by the intramural animal-welfare committee for animal experimentation of Chiesi Farmaceutici under protocol 449/2016-PR, and in compliance with European Directive 2010/63 UE, Italian D.Lgs 26/2014 and the revised "Guide for the Care and Use of Laboratory Animals".

Animal model

Female C57Bl/6 mice (7-8 weeks of age) were purchased from Envigo Italy (San Pietro al Natisone, Udine, Italy). The mice were housed in a pathogen-free facility and were provided food and water *ad libitum* for at least 5 days acclimatization prior to performing all experiments.

Sterile sunflower seeds and hydrogel were supplied as diet integration to prevent excessive body weight loss.

Animals were housed five per cage under standard conditions at our animal facility, in compliance with the procedures and principles outlined in the European Directive 2010/ 63 UE, Italian D.Lgs 26/2014 and the revised "Guide for the Care and Use of Laboratory Animals" (National Research Council Committee, US, 2011). All animal procedures were conducted in an AAALAC (Association for Assessment and

Accreditation for Laboratory Animal Care) certified facility at Chiesi Farmaceutici and were authorized by the Italian Ministry of Health with protocol number 449/2016-PR and by the internal AWB (Animal Welfare Body). All necessary measures were taken to minimize pain or discomfort to the animals, and Visual Analogue Scale (0-10) for pain assessment was evaluated daily by a designated veterinarian or trained technicians. VAS ≥6 and/or body weight loss ≥ 20% were considered as humane endpoints, as well as signs of dyspnoea or apathy evaluated by a designated veterinarian.

Briefly, mice were lightly anesthetized with 2.5% isoflurane delivered in induction chamber and positioned on the intubation stand. Lung fibrosis was induced in 42 mice using bleomycin hydrochloride (BLM, Baxter, 1 mg/kg) diluted in 50 μL saline (0.9%) via a double (day 0, 4) oropharyngeal administration (OA) using a micropipette as previously described,[22] whereas 15 mice received only saline. On day 7, a subgroup of BLM-treated mice was randomly selected to receive Nintedanib. From day 7 to 21, all animals were orally treated daily either with Nintedanib (NINT) at 60 mg/kg (Carbosynth Limited, Compton, UK) or vehicle (0.05% Tween80 in saline). On day 21, a subset of mice was imaged (n=10 SAL, n=16 BLM, n=10 NINT) and sacrificed for either invasive lung function testing or histological evaluation. The non-imaged mice were sacrificed for histological evaluation only on days 7 (n=5 SAL and n=6 BLM) and 21 (n=5 BLM and n=5 NINT). The experimental study plan is resumed in Figure S1.

METHOD DETAILS

Image acquisition

Quantitative multiphase cine respiratory images were acquired using a high temporal resolution flat-panel based micro-CT scanner Quantum GX (Revvity, Inc. Hopkinton, MA). Each mouse was anesthetized by inhalation of 2% isoflurane, which reduces respiratory rate and depth of ventilation, regularizing breathing.[36] Once an adequate depth of anesthesia was achieved, mice were placed in the supine body position on a scanner bed with a nose cone supplying 1.5 % isoflurane in oxygen. The forelimbs of mice were extended cephalad and fixed with a narrow strip of surgical tape to the nose cone to keep them out of the imaging field. The animal chest alignment within the field of view was performed under live-view radiographic observation at 0 and 90-degree gantry positions using X, Y, and Z axis motorized stage controls. The respiratory cycle length and rate were checked in the respiratory synchronization window of the scanner control software. If necessary, the level of isoflurane was decreased to 1.0 % to keep breathing rate above 120 breaths per minute. The respiratory signal trace, the respiratory cycle lengths and the respiratory rate were monitored during the acquisition.[37] To ensure sufficient data for the multiphase reconstructions, the X-ray detector of the scanner was set to acquire images with a temporal resolution of 16 ms using the respiratory high-speed mode. The X-ray tube voltage and current were set to 90 kV and 88 μA, respectively. A 0.5 mm Aluminum (Al) and 0.06 mm Copper (Cu) filter was used to remove low energy X-rays. Projection images were acquired over a single complete gantry rotation with a total rotation time of 4 minutes. The reconstructions quality was reviewed on the transaxial, coronal and sagittal views to be sure not to have blurred images from movements due to the low level of anesthesia. Upon completion or the scan, mice were removed from the scanner and allowed to recover fully from anesthesia under supervision.

Multiphase image reconstruction

The acquired data were reconstructed retrospectively throughout the entire respiratory cycle using the Multiphase Respiratory Reconstruction Module, MRRM (Binitio Biomedical, Inc., Ottawa, Ontario). All reconstructions were performed in axial slice orientation with the array size of 512 x 512 x 512 and with 50-μm isotropic voxels, producing around 26-32 reconstructed phases for each breathing cycle in mice with respiratory rate of 120-140 brpm.

Image analysis

The resulting multiphase image series were transferred to a dedicated analysis workstation and the airway lumen, left lung, right lungs, and pulmonary blood vessels were automatically segmented using a deep convolutional neural network (CNN) with U-Net architecture, previously validated in a mouse model of lung fibrosis, with a Dice score of about 0.97 on the test set.[15,18] Briefly, the segmentation module consists of a multi-resolution approach, based on a cascade of two CNN models: a low-resolution model trained on subsampled images for low-resolution pre-processing, and a high-resolution 2.5D CNN model combining three 2D CNNs that segment the input image in axial, sagittal and coronal planes separately and merge the segmentation results via voting. Each reconstructed respiratory phase was converted from grey levels to Hounsfield Units (HU). The conversion was based on a linear transformation, in which -1000 HU and +50 HU were set respectively as the density of air (average grey level value within the trachea) and heart (average gray level value of the heart), with the trachea and the heart delineated by the CNN. The processing time of a single reconstructed phase was approximately 1,5 minutes (57s per segmentation and 33s per densitometry analysis) using an NVIDIA Tesla P40 graphics card with CUDA = 6.1 computational capability, under the Windows operating system. The segmented respiratory phases are shown in Figure 1A.

Binary masks were then used to calculate the total lung volume and density values. At each respiratory phase x, gas volume (V_{gas}) that was breathed at the phase x was estimated from the total lung volume (Vol) as:

$$V_{gas}(x) = Vol(x) * \frac{MLA(x)}{-1000HU}$$

where MLA(x) is the mean lung attenuation at the respiratory phase x.

These time-varying scattered points covering the whole breathing cycle were fitted into a continuous curve, and reflected the dynamic change of the amount of air that was breathed during the respiratory cycle (Figure 1B). The gas flow, i.e. the air amount that was breathed per unit time, was calculated as the 1st derivative of the $V_{gas}(x)$ curve (Figure 1C). Finally, $V_{gas}(x)$ curve and its derivative, in analogy to flow-volume loops in spirometry, were plotted as a tidal breath flow-volume loop (Figure 1D), which has been previously reported as a compound measurement of lung function, including size of airways and mechanical characteristics of the lung, in the clinical setting.[38,39] Dynamic respiratory functional parameters were computed. Time variables were respiratory cycle (t_{TOT}), inspiratory time (t_I), expiratory time (t_E), inspiratory duty cycle (t_I / t_{TOT}), time to peak tidal inspiratory flow (tPTIF), time to peak tidal expiratory flow (tPTEF) and respiratory rate (RR, calculated as $60/t_{TOT}$). Volume parameters included end-inspiratory tidal volume (V_I), end-expiratory tidal volume (V_E) and tidal volume (V_T). Minute ventilation has been considered both as the product of tidal volume and respiratory rate, Min. ventilation = V_T x RR, and as the product of mean inspiratory flow and duty cycle, Min. ventilation = 60 x (V_T/t_I) x (t_I/ t_{TOT}). Peak and mean tidal inspiratory flow (PTIF, MTIF) and peak and mean tidal expiratory flow (PTEF, MTEF) were calculated as flow parameters. From the flow-volume curves, the inspiratory, expiratory and total loop areas were calculated (respectively $Area_I$, $Area_E$ and $Area_{TOT}$).

Pulmonary function testing

Invasive lung function testing was performed on day 21 (n=4 saline, n=7 BLM and n=5 NINT) after micro-CT lung imaging. Mice were deeply anesthetized intraperitoneally with a mixture of ketamine (100 mg/kg) and xylazine (10 mg/kg), tracheostomized, using an 18-gauge metal endotracheal cannula, and connected to the FlexiVent system (SCIREQ, Canada), set at a respiratory rate of 150 breaths/min, a tidal volume of 10 mL/kg and a positive end-expiratory pressure of 3 cmH2O. To prevent spontaneous breathing mice also received Pancuronium bromide 1 mg/kg intraperitoneally. The following parameters were measured: total inspiratory capacity (IC), lung tissue damping (G) and lung tissue elastance (H) using Primewave-8 forced oscillation; static compliance (Cst) using the pressure volume curve and dynamic compliance (Crs) using Snapshot 120 perturbation. FlexiVent software version 8.1 was used to perform the perturbations. Consecutive measurements were performed until three acceptable measurements (coefficient of determination > 0.95) were recorded in each individual mouse. The average of these three measurements was used for the analysis.

Histological lung fibrosis quantification and bronchoalveolar lavage

Mice were sacrificed on day 7 (n=5 SAL and n=6 BLM) and 21 (n=6 SAL, n=14 BLM and n=10 NINT) by anesthetic overdose followed by bleeding from the abdominal aorta. for histological analysis. As shown in Figure S1, histological analysis was performed both in non-imaged mice on days 7 (n=5 SAL and n=6 BLM) and 21 (n=5 BLM and n=5 NINT) as well as in a subset of imaged mice, that did not perform Flexivent (n=6 saline, n=9 BLM and n=5 NINT) .

A cannula through the trachea was inserted to collect Bronchoalveolar lavage fluid (BALF) and gently washed with 0.6 mL sterile solution [Hank's balanced salt solution 1X; ethylenediaminetetraacetic acid 10 mM; 4-(2-hydroxy-ethyl)-1-piperazineethansulphonic acid 10 mM; distilled water]. The cell pellet was resuspended in 0.2 ml of PBS and white blood cells (WBC) were counted with an automated cell counter (Dasit XT 1800J, Sysmex).[40]

For histological determination, lungs were exposed, inflated with 0.6 ml of 4% formaldehyde buffered solution, excised and fixed for 24h before embedding in paraffin. From each mouse, lung sections of 5 μm were cut with a rotary microtome (Reichert-Jung 1150/ Autocut), following the dorsal plane.

Three sections for each lung sample were stained with Masson's trichrome (TM) and Hematoxylin and eosin (H&E) and digitalized by NanoZoomer S-60 Digital slide scanner (Hamamatsu, Japan).

Lung morphological parenchyma changes were graded semi-quantitatively according to the scale defined by Ashcroft[41] modified by Hübner et al.[42] and adjusted for murine samples,[43] by two independent researchers blinded to the experimental design. The final score was expressed as the mean of the individual scores observed across all microscopic fields.

QUANTIFICATION AND STATISTICAL ANALYSIS

All statistical analyses were performed using Prism 8 software (GraphPad Software Inc., San Diego, California, United States). One-way analysis of variance was applied to compare μCT-derived dynamic respiratory parameters and PFT outcome measures between groups (saline, BMT and Nintedanib-treated animals) separately on day 7 and 21. Nonparametric Kruskal–Wallis analysis of variance on ranks was applied, if equal variance test and/or normality test failed. If differences were identified, Dunnett's or Dunn's multiple comparison post hoc test was performed. The correlation between μCT-derived dynamic respiratory parameters, PFT-measured functional and mechanical parameters and the Ashcroft score was assessed by calculating Spearman correlation coefficients. Values in the main body and tables are reported as medians (25–75th percentiles). A sample size of 6 and 7 animals/group is required at the two timepoint respectively to observe significant differences in imaging-derived functional parameters (significance level of 5% and statistical power of 90%).[18] $p < 0.05$ was considered statistically significant.